DYN-1 regulates SPD-2 and PLK-1 localization and mitotic spindle pole organization

Carter Dierlam[1], Stephanie Held[2], Jiya Hastings[2], Livinus Anyanwu[3], Robert H. Newman[2], and Jyoti Iyer[2]*

[1]Department of Cell Biology and Molecular Genetics, University of Maryland College Park, College Park, MD 20742, [2]Department of Biology, North Carolina Agricultural and Technical State University, Greensboro, NC 27411, and [3]Department of Chemistry and Biochemistry, University of Tulsa, Tulsa, OK 74104.

Number of characters = 19,747

Running title: *DYN-1 regulates SPD-2 and PLK-1*

*To whom correspondence should be addressed:

Jyoti Iyer

Email: jgiyer@ncat.edu; Tel. (336) 285-4573

Keywords: dynamin, PLK-1, SPD-2, mitosis, midbody, centrosome

ABSTRACT

Accurate cytokinesis is essential for genome stability. Although dynamin is best known for its role in vesicular trafficking, its functions during mitosis remain unclear. Here, we identify a mitotic role for the *C. elegans* dynamin homolog DYN-1 in regulating spindle assembly and the localization of the key mitotic regulators SPD-2 and PLK-1. Depletion of DYN-1 results in enlarged metaphase spindle poles and increased centrosomal SPD-2 and PLK-1 levels. These effects likely depend on DYN-1's vesicular trafficking activity. Additionally, a subset of DYN-1–depleted embryos exhibit altered PLK-1 localization at the midbody during late mitosis, correlating with midbody assembly defects. Together, these findings establish DYN-1 as a previously unrecognized regulator of spindle pole organization and early midbody assembly.

SIGNIFICANCE STATEMENT

Dynamin is primarily known for its function in endocytosis, but its involvement in mitosis is not well defined. This study shows that dynamin helps organize mitotic spindle poles, ensures proper centrosome localization of SPD-2 and PLK-1, and supports early steps of midbody assembly in *C. elegans* embryos. These findings reveal a previously unrecognized mitotic role for dynamin and suggest new links between membrane dynamics, spindle organization, and the cytokinetic machinery.

38 **INTRODUCTION**

39 Accurate cell division is essential for proper chromosome segregation, and mitotic errors
40 can lead to aneuploidy—a distinguishing feature of many cancers (Levine and Holland, 2018).
41 Understanding the molecular mechanisms that regulate mitosis is therefore critical. The GTPase
42 dynamin is a large ~100 kDa protein that is best known for its role in the scission of endocytic
43 vesicles (Hinshaw, 2000; Praefcke and McMahon, 2004). *C. elegans* possesses a single classical
44 dynamin encoded by the *dyn-1* gene (Clark *et al*., 1997). Interestingly, some of the earliest
45 studies identified dynamin as a microtubule-binding protein (Paschal *et al.*, 1987; Shpetner and
46 Vallee, 1989). However, dynamin's function in microtubule-associated processes such as spindle
47 assembly and midbody organization during mitosis is not well understood. While DYN-1 was
48 shown to localize to the midbody (Thompson *et al.*, 2002), and mediate membrane remodeling
49 during the late stages of abscission (König *et al.*, 2017), its potential role in early midbody
50 assembly remains unexplored.

51 The coiled-coil protein SPindle Defective 2 (SPD-2) (the *C. elegans* homolog of human
52 CEP192) is essential for proper centrosome biogenesis and spindle assembly during mitosis
53 (O'Connell *et al.*, 2000; Kemp *et al.*, 2004; Pelletier *et al.*, 2004; Gomez-Ferreria *et al.*, 2007,
54 Zhu *et al.*, 2008). SPD-2 levels at the centrosomes are regulated by proteins including SAS-7,
55 SPD-5, DHC-1 and AIR-1, among others (Sugioka *et al.*, 2017; Kemp *et al.*, 2004; Pelletier *et*
56 *al.*, 2004). Proper levels of centrosome-associated SPD-2 are required for proper centriole
57 duplication, pericentriolar material (PCM) organization and spindle assembly (O'Connell *et al.*,
58 2000; Kemp *et al.*, 2004; Pelletier *et al.*, 2004). SPD-2 directly binds to the kinase Polo-like
59 kinase 1 (PLK-1) to recruit the kinase to the centrosomes (Boxem *et al.,* 2008; Decker *et al.,*
60 2011).

61 PLK1 is a mitotic master regulator that is essential for several mitotic processes including
62 mitotic entry, centrosome dynamics, chromosome congression, chromosome alignment and
63 cytokinesis (Petronczki *et al.,* 2008; Archambault and Glover, 2009; Zitouni *et al.,* 2014). PLK1
64 exhibits a dynamic localization pattern at different stages of mitosis. During early mitosis, PLK1
65 localizes prominently to the centrosomes, and the kinetochores. At anaphase, it re-localizes to the
66 spindle midzone and at telophase, it becomes enriched at the midbody (Golsteyn *et al.,* 1995; Lee
67 *et al.,* 1995; Arnaud *et al.,* 1998; Barr *et al.*, 2004; Petronczki *et al.,* 2008; Schmucker and
68 Sumara, 2014). The timely localization of PLK1 to various cellular components is essential for
69 its different important roles during mitosis. Importantly, removal of PLK1 from the centrosomes
70 is required for proper mitotic progression (Kishi *et al.,* 2009). Although the kinase activity of
71 PLK1 is thought to be required for PLK1 removal from the centrosomes (Kishi *et al.,* 2009), the
72 mechanism by which PLK1 is removed from the centrosomes remains unclear.

73 **RESULTS AND DISCUSSION**

74 ***dyn-1* depletion results in abnormal metaphase spindle pole assembly and increased levels**
75 **of SPD-2**

76 To determine the effect of DYN-1 depletion in *C. elegans* embryos, we knocked down
77 endogenous DYN-1 using *RNAi* (Supplemental Figure S1, A and B). Interestingly, DYN-1–
78 depleted embryos (n=20) were noticeably smaller than controls (n=23), exhibiting a reduced
79 average cytoplasmic area (~906 μm^2 vs. ~1200 μm^2; $p < 0.0001$) (Supplemental Figure S1, C
80 and D). DYN-1 was previously shown to localize to the mitotic spindle at metaphase, suggesting
81 a potential role in metaphase spindle assembly (Thompson *et al.,* 2002). To determine the effect
82 of DYN-1 depletion on metaphase spindle assembly, we examined the effect of DYN-1 depletion
83 on spindle pole size using mCherry::tubulin as a proxy (Figure 1). Upon measuring spindle pole

84 area, we determined that DYN-1-depleted embryos (n=58 spindle poles) exhibited larger spindle
85 poles than control (*smd-1(RNAi)*)-depleted embryos (n=53 spindle poles; p=0.0018) (Figure 1, A
86 and B). Specifically, the average spindle pole area of control RNAi embryos was 14.6 μm^2 while
87 that of *dyn-1(RNAi)* embryos was 17.36 μm^2. Thus, our data have identified a novel role for the
88 endocytic protein DYN-1 in regulating metaphase spindle pole assembly. An important regulator
89 of spindle pole and centrosome size is the PCM protein SPD-2 (O'Connell *et al.*, 2000; Kemp *et*
90 *al.*, 2004; Pelletier *et al.*; Decker *et al.,* 2011). Therefore, we asked whether SPD-2 levels at the
91 centrosomes were altered between control RNAi and *dyn-1(RNAi)* treated embryos. Our analysis
92 indicated that centrosome-associated SPD-2 levels were significantly increased ~1.7-fold upon
93 DYN-1 depletion (Figure 1, C and D; n=66 for *dyn-1(RNAi)*; n=60 for controls; $p < 0.0001$).
94 **DYN-1 depletion increases levels of centrosome-associated PLK-1**
95 Because SPD-2 directly binds to PLK-1 and recruits it to centrosomes (Boxem *et al.,* 2008;
96 Decker *et al.,* 2011), and SPD-2 levels increase upon DYN-1 depletion (Figure 1, C and D), we
97 next asked whether PLK-1 also becomes elevated at centrosomes under these conditions. To
98 determine if DYN-1 depletion affects centrosomal PLK-1, we performed live imaging on a strain
99 co-expressing mCherry::tubulin and CRISPR-tagged endogenous PLK-1::sfGFP (Martino *et al.,*
100 2017). We then knocked down endogenous DYN-1 in this strain using *RNAi* and performed live
101 imaging of control (*smd-1*(*RNAi)*) and *dyn-1(RNAi)* treated embryos using spinning-disk
102 confocal microscopy. Consistent with our hypothesis, our analysis revealed that PLK-1 levels at
103 the centrosomes were significantly elevated upon DYN-1 depletion (Figure 2, A and B).
104 Specifically, we found that PLK-1 intensity was ~2.5-fold higher in *dyn-1(RNAi)* embryos
105 (n=52) than controls (n=58; $p < 0.0001$) (Figure 2, A and B).

106 The *dyn-1(ky51)* GTPase mutant, which perturbs vesicular trafficking (Clark *et al.*, 1997;
107 Grant and Hirsch, 1999), also exhibited increased centrosomal PLK-1 (Figure 2). Specifically,
108 PLK-1 levels were on average elevated ~1.85-fold at *dyn-1(ky51)* centrosomes (n=46
109 centrosomes) as compared with control centrosomes (n=44 centrosomes; $p<0.0001$) (Figure 2, C
110 and D). These data indicate that the vesicular trafficking function of DYN-1 is required for its
111 regulation of centrosome-associated PLK-1 levels. Furthermore, these data also confirm the
112 specificity of our *dyn-1(RNAi)* phenotype.
113 To determine if total cellular levels of PLK-1 are altered between control and *dyn-*
114 *1(ky51)* embryos, we next measured PLK-1::sfGFP fluorescence intensity within the anterior and
115 posterior cytoplasm of metaphase embryos (Supplemental Figure S2). We reasoned that if total
116 PLK-1 levels are increased upon impairing DYN-1 function, we should see a proportional
117 increase in cytoplasmic PLK-1 fluorescence in the *dyn-1(ky51)* embryos. Our analysis revealed a
118 modest ~7% increase in PLK-1 levels in the anterior and posterior cytoplasm of *dyn-1(ky51)*
119 embryos as compared with controls ($p=0.0234$ (anterior), $p=0.0318$ (posterior)) (Supplemental
120 Figure S2). Given that PLK-1 levels at metaphase centrosomes increase by ~1.85-fold in *dyn-*
121 *1(ky51)* embryos (Figure 2, C and D), this modest ~1.07-fold increase in cytoplasmic PLK-1 is
122 unlikely to fully explain the elevated centrosome-associated PLK-1 levels observed in these
123 mutants.

124 **PLK-1 persists at the centrosomes following DYN-1 depletion in a subset of embryos**
125 **during the later stages of mitosis**

126 PLK-1 exhibits a spatially and temporally regulated localization pattern during different stages of
127 mitosis (Chase *et al.,* 2000; Budirahardja and Gönczy, 2008; Martino *et al.,* 2017). It transitions
128 from its location at the centrosomes and the kinetochores during early mitosis, to the spindle

129 midzone and the midbody during late mitosis (Chase *et al.,* 2000; Budirahardja and Gönczy,
130 2008; Martino *et al.,* 2017). While performing live imaging, we noticed several embryos where
131 PLK-1 appeared to persist at the centrosomes (specifically at the PCM) during the later stages of
132 mitosis (Figure 3A). To quantify this phenotype, we analyzed PLK-1::sfGFP fluorescence
133 intensity at anterior centrosomes at different cell cycle stages in both control RNAi and *dyn-*
134 *1(RNAi)* treated embryos (Figure 3; Supplemental Figure S3). Note that we measured PLK-
135 1::sfGFP at anterior centrosomes only because cytoplasmic background is more uniform there; in
136 contrast, the posterior cytoplasm contains punctate, uneven PLK-1 that makes measurements
137 unreliable. Our quantitative analysis revealed that there was no PLK-1 detectable at any of the
138 control centrosomes analyzed at 35 seconds post early telophase (n=29 centrosomes) (Figure 3,
139 A and B; Supplemental Figure S3). In contrast, in 35% of the centrosomes from *dyn-1(RNAi)*
140 treated embryos (9 out of 26 centrosomes), PLK-1 was still detectable at the centrosomes at this
141 stage (p=0.0005) (Figure 3, A and B; Supplemental Figure S3).
142 We also noted a statistically significant increase in centrosome-associated PLK-1::sfGFP
143 upon *dyn-1(RNAi)* (n=26 centrosomes) as compared with controls (n=29 centrosomes) via an
144 unpaired two-tailed t-test at early anaphase (p<0.0001), late anaphase (p=0.0004) as well as in
145 early telophase (p=0.0094) (Supplemental Figure S3). These data indicate that a pool of PLK-1
146 tends to persist at the centrosomes of DYN-1-depleted embryos during the later stages of mitosis.
147 **DYN-1-depleted embryos exhibit abnormal midbody formation**
148 Since DYN-1 has a known role in cytokinesis and localizes to the midbody (Thompson *et al.,*
149 2002), we analyzed midbody formation in DYN-1-depleted embryos. Intercellular bridge (IB)
150 assembly, assessed using mCherry::tubulin fluorescence, served as a proxy for midbody
151 formation (Hu *et al.*, 2012; Green *et al.,* 2013; König *et al.*, 2017). We noted that all of the

152 control RNAi embryos (n=19 embryos) exhibited a normal tubulin-intense IB during telophase
153 (Figure 4, A (white arrows) and B). In contrast, 50% of the *dyn-1(RNAi)* embryos (12 out of 24
154 embryos) did not exhibit any detectable IB during telophase (Figure 4, A (bottom panel) and B).
155 Interestingly, 46% of the *dyn-1(RNAi)* embryos exhibited a structurally abnormal IB that either
156 started forming outside the reference time-window for normal IB assembly (normal IB started
157 forming between 175 to 350 seconds post-metaphase) or exhibited defects in IB assembly
158 dynamics (Figure 4, A (middle panel) and B). Importantly, the *dyn-1(ky51)* allele also exhibited
159 mild defects in IB assembly (Figure 4B), demonstrating the specificity of this phenotype. While
160 previous ultrastructural analysis identified a role for DYN-1 in membrane remodeling during the
161 late stages of abscission (König et al., 2017), our study identifies a novel requirement for DYN-1
162 in regulating midbody organization during the initial stages of this process. Together, these data
163 suggest that DYN-1 function is required for proper midbody assembly.

164 **PLK-1 localization to the midbody is defective in DYN-1-depleted embryos**

165 Given that PLK-1 persists at the centrosomes through late mitosis in a subset of DYN-1-depleted
166 embryos (Figure 3), we hypothesized that this retention might correlate with abnormal PLK-1
167 dynamics at the midbody. To investigate this, we analyzed PLK-1 localization using two
168 complementary approaches: a time-matched analysis and an event-matched analysis. The time-
169 matched analysis (Figure 5, A and B) examined whether PLK-1 localized to the midbody during
170 the standard developmental window when IB formation begins (175–350 seconds post-
171 metaphase). Conversely, the event-matched analysis evaluated PLK-1 recruitment specifically
172 when an IB eventually formed, regardless of timing.

173 Our time-matched analysis revealed that PLK-1 failed to localize to the midbody in 83%
174 of *dyn-1(RNAi)* embryos (n = 24), compared to 100% localization in controls (n = 19; $p <$

175 0.0001; Figure 5A). To distinguish whether this reduction was simply due to a failure in
176 midbody formation, we performed an event-matched analysis restricted to *dyn-1(RNAi)* embryos
177 where an IB-like structure was present (n = 12). Importantly, PLK-1 localized to these formed
178 midbodies to varying degrees in all cases: 42% showed relatively normal accumulation, while
179 58% exhibited fragmented, weak, or near-background signals (Figure 5, A and C; p=0.0003).
180 Together, these data demonstrate that even when a midbody successfully forms following *dyn-1*
181 depletion, PLK-1 recruitment is frequently altered rather than entirely absent. Notably, due to
182 inconsistent background signals resulting from polarity defects in *dyn-1(RNAi)* embryos, we
183 were unable to reliably quantify PLK-1::sfGFP fluorescence intensity at midbodies, as these
184 background fluorescence fluctuations often led to inconsistent measurements.

185 In summary, our studies have identified a new role for the endocytic protein DYN-1 in
186 regulating metaphase spindle assembly, early midbody assembly and the localization of the
187 mitotic proteins SPD-2 and PLK-1. Specifically, we find that upon DYN-1 depletion, SPD-2 and
188 PLK-1 accumulate at the centrosomes in metaphase and this is associated with aberrant
189 metaphase spindle pole assembly. Furthermore, while PLK-1 is normally removed from the
190 centrosomes during late mitosis, upon DYN-1 depletion, we find that PLK-1 persists at a subset
191 of centrosomes during the later stages of mitosis.

192 Based upon our data, we propose a model whereby DYN-1 regulates the levels of SPD-2
193 and PLK-1 at metaphase centrosomes, potentially through a vesicular trafficking mechanism.
194 DYN-1 depletion leads to elevated SPD-2 levels at metaphase centrosomes, and because SPD-2
195 is a known upstream recruiter of PLK-1 (Boxem *et al.*, 2008; Decker *et al.*, 2011), this increase
196 in SPD-2 is accompanied by increased PLK-1 accumulation at centrosomes. The elevated levels
197 of these PCM components are associated with aberrant spindle pole assembly. In late mitosis,

198 DYN-1 depletion also disrupts the normal relationship between midbody formation and PLK-1
199 accumulation at the IB: embryos frequently fail to assemble a midbody, and even in cases where
200 a midbody-like structure does form, PLK-1 enrichment is often fragmented or reduced. While we
201 cannot yet distinguish whether altered PLK-1 midbody localization reflects defective midbody
202 assembly, impaired PLK-1 recruitment, or a combination of both, our findings indicate that
203 DYN-1 is required for coordinating the proper redistribution of PLK-1 between centrosomes and
204 the midbody.

205 The defects in midbody assembly were more pronounced in *dyn-1(RNAi)* embryos than in
206 *dyn-1(ky51)* mutants. Correspondingly, PLK-1::sfGFP enrichment at metaphase centrosomes
207 was higher following *dyn-1(RNAi)* (~2.5-fold) compared to *dyn-1(ky51)* (~1.85-fold). These
208 observations suggest that *dyn-1(ky51)* may be a hypomorphic allele. Alternatively, DYN-1 may
209 regulate these processes through mechanisms other than its role in vesicular trafficking. Future
210 studies should investigate these potential roles, including whether DYN-1 physically interacts
211 with PLK-1 to facilitate its recruitment or turnover. Rescue approaches using hypomorphic *plk-1*
212 alleles may also help clarify the contribution of PLK-1 dysregulation to causality of the observed
213 defects, but such experiments are beyond the scope of the present work.

214 Since our studies also uncovered the regulation of centrosome-associated SPD-2 levels
215 by DYN-1, an important next step is to determine the specific mechanism of this regulation.
216 Since SPD-2 is one of the upstream components of the PCM assembly pathway (Kemp *et al.*,
217 2004), future studies will also be directed to determine if other PCM protein levels at the
218 centrosomes are also altered upon DYN-1 depletion. Investigating these broader effects will
219 clarify whether the role of DYN-1 is specific to the SPD-2/PLK-1 axis or if it influences
220 centrosome composition and mitotic spindle assembly more generally.

221 **MATERIALS AND METHODS**

222 ***C. elegans* strains growth and maintenance**

223 All *C. elegans* strains described in this study were grown and maintained using standard
224 techniques on OP50 seeded Modified Youngren's Only Bacto-peptone (MYOB) agar plates at
225 20ºC (the strains were shifted to other assay-specific temperatures as needed).

226 ***C. elegans* strains and genetic crosses**

227 The wild-type N2 strain and the OD2425 strain expressing PLK-1::sfGFP (*plk-1(lt18[plk-*
228 *1::sfGFP]::loxp) III)* (Martino *et al.,* 2017) were obtained from the *Caenorhabditis Genetics*
229 *Center* (CGC). The OC908 strain (*bsSi30[pCW9: unc-119(+) pcdk-11.2::sfgfp::his-58::cdk-11.2*
230 *3′ UTR] II; bsIs20[pNP99: unc-119(+) tbb-1p::mCherry::tbb-2::tbb-2 3′-UTR]; bsIs2[pCK5.5:*
231 *Ppie-1::gfp::spd-2]*) and the OC779 strain (*bsSi15[pKO109: spd-2p-spd-2::mCherry::spd-2 3′-*
232 *utr, unc-119(+)] I; bsSi30[pCW9: unc-119(+) pcdk-11.2::sfgfp::his-58::cdk-11.2 3′ utr] II; unc-*
233 *119(ed3) III*) were obtained from Dr. Kevin O'Connell's laboratory at NIDDK, NIH. The
234 mCherry::tubulin–expressing strain IYR028 (*bsIs20[pNP99: unc-119(+) tbb-1p::mCherry::tbb-*
235 *2::tbb-2 3′-UTR]*) was generated in our laboratory by crossing OC908 hermaphrodites with N2
236 males and isolating progeny carrying only the mCherry::tubulin transgene. Following this,
237 mCherry::tubulin expressing males were generated from the IYR028 strain by heat shock at 30°C
238 for 6 hours. These mCherry::tubulin males from the IYR028 strain were then crossed with PLK-
239 1::sfGFP expressing hermaphrodites from the OD2425 strain to generate the IYR038 strain
240 (*bsIs20[pNP99: unc-119(+) tbb-1p::mCherry::tbb-2::tbb-2 3′-UTR]; plk-1(lt18[plk-*
241 *1::sGFP]::loxP) III)* which was homozygous for both mCherry::tubulin and PLK-1::sfGFP. This
242 strain was validated for homozygosity of the two loci by confocal microscopy. The IYR035
243 strain (*dyn-1(luv35[ky51]) X*) was generated by CRISPR/Cas9 editing as described previously

244 (Paix *et al.,* 2015; Paix *et al.,* 2016; Iyer *et al.,* 2018; Smith *et al.*, 2020). This strain was
245 confirmed by both PCR and restriction digestion with Pst1 followed by agarose gel
246 electrophoresis as well as by DNA sequencing. The IYR043 strain (*bsIs20[pNP99: unc-119(+)*
247 *tbb-1p::mCherry::tbb-2::tbb-2 3'-UTR]; plk-1(lt18[plk-1::sfGFP]::loxP) III; dyn-*
248 *1(luv35[ky51]) X*) was homozygous for the *dyn-1(ky51)* mutation, mCherry::tubulin and PLK-
249 1::sfGFP. The IYR044 strain (*bsIs20[pNP99: unc-119(+) tbb-1p::mCherry::tbb-2::tbb-2 3'-*
250 *UTR]; plk-1(lt18[plk-1::sfGFP]::loxP) III; dyn-1(+) X*) was homozygous for mCherry::tubulin,
251 PLK-1::sfGFP and wild-type for *dyn-1*. The IYR043 and IYR044 strains were both generated by
252 crossing IYR035 hermaphrodites with IYR038 males (the males were made by heat shock at
253 30°C for 6 hours). Both these strains were validated by confocal microscopy for homozygosity of
254 the fluorescent markers (mCherry::tubulin and PLK-1::sfGFP). PCR and Pst1 digestion followed
255 by agarose gel electrophoresis as well as by DNA sequencing was used to confirm homozygosity
256 of the *dyn-1(ky51)* mutation (IYR043) and wild-type *dyn-1* (IYR044).

257 **CRISPR/Cas9 editing**

258 CRISPR/Cas9 genome editing utilizing assembled ribonucleoprotein complexes and a linear
259 DNA repair template (Paix *et al.,* 2015; Paix *et al.,* 2016) was performed to generate the IYR035
260 strain (*dyn-1(luv35[ky51]) X*) according to the protocols detailed in Iyer *et al.* (2018) and Smith
261 *et al.* (2020). The sequences of the editing reagents used to create this strain are as follows:
262 *dyn-1(ky51)* crRNA: 5'- TGAATAAGCTGCAAAATAAG -3'
263 *dyn-1(ky51)* repair template (silent mutations introduce a Pst1 restriction site): 5'-
264 AGACTTCTTGCCACGTGGATCAGGAATCGTAACACGTCGTTCATTGATCCTGCAGCT
265 TATTCAAGATCGCAATGAGTACGCCGAGTTCCTAC -3'
266 *dyn-1(ky51)* screening primers:

267 *dyn-1(ky51)* forward: 5'- CGTTGATCCCTGTGATCAAT – 3'

268 *dyn-1(ky51)* reverse: 5'- TTTCAGATGCTCAAATCATCC – 3'

269 ***RNAi* by feeding**

270 HT115 bacteria expressing the *dyn-1(RNAi)* construct were purchased from Horizon Discovery
271 Ltd. (Lafayette, CO) while HT115 bacteria expressing the *smd-1 RNAi* construct (control) were
272 obtained from Dr. Kevin O'Connell's laboratory (NIDDK, Bethesda, MD). HT115 *E. coli*
273 transformed with either control (*smd-1(RNAi)*) or *dyn-1(RNAi)* plasmids were grown on MYOB
274 plates supplemented with 100 µg/ml carbenicillin and 2 mM Isopropyl β- d-1-
275 thiogalactopyranoside (IPTG) as described previously (Kamath and Ahringer J 2003; Iyer *et al.,*
276 2022). Briefly, L4-stage *C. elegans* from the IYR038 strain were transferred onto *RNAi* plates
277 and incubated at 25 ºC for 24 to 36 hours. Gravid adults from these plates were then dissected to
278 release their embryos and 1-cell stage embryos were analyzed by confocal live imaging.

279 **Conditions for wild-type and *dyn-1(ky51)* worms**

280 Starved plates with the IYR043 (*dyn-1(ky51)*) and IYR044 (wild-type *dyn-1*) strains were
281 washed with M9 buffer and used to seed large 10 cm MYOB plates. These plates were placed at
282 26 ºC until L4s appeared. 100 to 125 L4s were picked from each plate and transferred onto new
283 individual 10 cm MYOB plates at 26 ºC overnight. Embryos from both strains were imaged the
284 next day using a spinning-disk confocal microscope.

285 **Sequence of *dyn-1(RNAi)* construct**

286 The commercially purchased *dyn-1(RNAi)* construct (Horizon Discovery Inc.) was subjected to
287 whole plasmid sequencing (Plasmidsaurus). The targeting sequence was found to be as follows:
288 5'-
289 ATGTCGTGGCAAAACCAGGGAATGCAGGCGTTGATCCCTGTGATCAATCGTGTCCAG

290 GACGCCTTCTCCCAGCTGGGCACATCTGTCAGCTTCGAACTTCCACAGATCGCCGTC

291 GTCGGAGGACAGTCCGCTGGAAAGTCGTCGGTGCTGGAGAATTTTGTCGGAAAAGA

292 CTTCTTGCCACGTGGATCAGGAATCGTAACACGTCGTCCACTTATTTTGCAGCTTATT

293 CAAGATCGCAATGAGTACGCCGAGTTCCTACACAAGAAGGGTCATCGCTTTGTGGAT

294 TTTGATGCAGTTCGGAAAGAGATTGAGGATGAGACTGATCGTGTCACTGGACAGAA

295 TAAGGGAATCAGTCCACATCCAATCAACTTGCGTGTCTTTTCTCCAAATGTTCTAAAT

296 CTGACACTCATCGATTTGCCCGGTCTCACAAAAGTGCCCGTCGGAGATCAACCAGCA

297 GATATTGAGCAACAGATCCGTGACATGATTCTCACATTCATCAACCGTGAGACTTGC

298 CTCATTCTTGCCGTCACTCCGGCCAACAGCGATCTCGCCACTTCGGATGCGTTGAAA

299 CTTGCGAAGGAAGTCGATCCACAGGGTCTTCGCACGATTGGAGCCCTCACCAAACTT

300 GACTTGATGGACGAGGGAACCGATGCTCGCGAGATCCTCGAGAACAAGCTGTTCAC

301 ACTTCGTCGTGGCTACGTCGGAGTTGTCAATCGTGGGCAGAAGGATATTGTCGGTCG

302 CAAGGATATTAGAGCTGCTTTGGACGCCGAGAGAAAGTTCTTCATCTCACACCCATC

303 CTACCGACATATGGCTGATCGGTTGGGAACAAGCTACCTTCAACACACTCTTAATCA

304 ACAGCTCACCAATCATATCCGTGATACACTGCCAACACTTCGTGATAGTCTTCAAAA

305 GAAGATGTTTGCTATGGAAAAGGATGTGGCCGAGTACAAGAACTACCAGCCAAATG

306 ATCCAGGCCGCAAGACCAAGGCTCTTTTGCAAATGGTTACCCAGTTCAATGCTGACA

307 TTGAGCGCTCCATTGAAGGTTCCTCTGCAAAGCTGGTTTCAGCCAATGAGCTCAGTG

308 GAGGAGCCCGTATCAATCGGCTTTTCCATGAGCGTTTCCCATTTGAGATTGTTAAAA

309 TGGAAATTGACGAGAAAGAAATGCGCAAAGAAATCCAGTATGCCATCAGAAACATT

310 CACGGTATCCGCGTCGGTCTCTTCACTCCGGATATGGCGTTTGAGGCAATTGCCAAA

311 AAGCAAATCACCCGTCTGAAGGAGCCATCGTTGAAATGCGTTGATCTGGTGGTCAAC

312 GAGTTGGCTAATGTGATCAGACAGTGCGCTGACACTATGGCTAGATATCCACGTCTT

313 CGTGACGAGCTGGAAAGAATCGTCGTCTCGCATATGCGTGAACGTGAGCAAATTGC

314 CAAGCAGCAAATTGGGCTCATTGTTGACTACGAACTCGCTTATATGAACACAAACCA

315 TGAGGATTTCATTGGATTCAGCAATGCTGAAGCAAAAGCCTCCCAAGGACAATCAG

316 CGAAGAAGAATCTTGGAAACCAGGTGATCAGAAAGGGCTGGCTCTCACTGAGCAAC

317 GTATCGTTTGTGCGTGGCTCCAAGGACAATTGGTTTGTGCTCATGTCGGACAGTTTG

318 AGTTGGTACAAAGATGATGAGGAGAAGGAGAAGAAGTACATGCTCCCATTGGATGG

319 TGTCAAGCTGAAGGATATTGAGGGTGGATTTATGTCTCGTAACCACAAGTTTGCTCT

320 GTTCTACCCCGACGGAAAGAACATCTACAAGGATTACAAGCAGCTTGAGTTGGGAT

321 GCACCAATTTGGACGAAATTGATGCGTGGAAGGCTTCATTCTTGCGTGCTGGTGTCT

322 ATCCAGAAAAGCAGAAGGCACAGGAAGATGAGTCCCAACAAGAGATGGAGGATAC

323 CTCGATTGATCCACAACTTGAGAGACAGGTGGAGACAATCCGTAATTTGGTTGATTC

324 CTACATGAGAATCATTACCAAGACAATTAAGGACCTGGTTCCAAAGGCGGTGATGC

325 ATTTGATTGTTAACCAGACAGGTGAGTTCATGAAAGATGAACTTTTGGCCCATCTCT

326 ACCAATGCGGCGACACTGATGCTCTCATGGAGGAATCTCAAATAGAAGCCCAGAAG

327 CGCGAGGAGATGCTCCGAATGTACCATGCTTGCAAGGAGGCGCTCCGCATTATCTCT

328 GAAGTCAACATGAGCACCCTTGGCGACCAGCCGCCGCCATTGCCGATGTCTGACTAC

329 CGCCCACACCCATCTGGACCTTCACCGGTGCCGCGTCCGGCTCCTGCTCCACCAGGC

330 GGACGTCAGGCCCCAATGCCACCACGCGGAGGACCCGGTGCCCCACCACCACCAGG

331 CATGAGACCACCACCAGGTGCGCCAGGAGGCGGCGGTGGCATGTACCCACCGTTGA

332 TTCCAAC- 3’

333 ***dyn-1* RT-PCR**

334 The protocol by Ly *et al.,* 2015 was used to extract RNA from either 50 or 100 control and *dyn-*

335 *1(RNAi)* treated gravid adult worms. One modification to the protocol involved freezing the

336 worms in the TRIzol reagent (Thermo Fisher Scientific, Catalog #15596018) at –80 °C and
337 storing them until the day of the RNA extraction. RT-PCR was performed using the Qiagen
338 OneStep RT-PCR kit (Qiagen Inc., Catalog # 210210) following the manufacturer's instructions.
339 The primers used for the RT-PCR were as follows:
340 *dyn-1* RT-PCR forward: 5'- TGTCGGAAAAGACTTCTTGC – 3'
341 *dyn-1* RT-PCR reverse: 5'- TGTCAGATTTAGAACATTTGG – 3'
342 Primers sequences targeting the *act-1* gene (loading control) were obtained from Ly *et al.* (2015).
343 act1f*:* 5'- ACGCCAACACTGTTCTTTCC – 3'
344 act1r*:* 5'- GATGATCTTGATCTTCATGGTTGA – 3'
345 Band intensities for all RT-PCR samples were quantified using the open-source software Fiji
346 (Schindelin *et al.,* 2012).
347 ***C. elegans* embryo live imaging using a spinning-disk confocal microscope**
348 **For imaging embryos from the IYR038 and OC779 strains depicted in Figure 1:**
349 *C. elegans* embryos obtained from dissected *smd-1(RNAi)* (control) and *dyn-1(RNAi)* worms
350 were imaged using an Olympus Yokagawa X1 spinning-disk confocal microscope as described
351 previously (Bergwell, Smith, *et al.,* 2023) with a few alterations. Timelapse imaging was
352 performed using the cellSens software (Olympus America Inc.) by taking 1.5 µm Z-stacks every
353 ~75 seconds at a 60X magnification with a 1.42 numerical aperture (NA) objective using a Prime
354 95B CMOS camera. To enable quantitative analysis, all images were captured at the same laser
355 intensity [(50% laser intensity for both 561 nm and 488 nm channels for IYR038) and (60% laser
356 intensity for 561 channel and 35% laser intensity for 488 channel for OC779)] and exposure time
357 (700 msec exposure time for both 561 nm and 488 nm channels for both strains). All brightness

358 and contrast adjustments were applied equally for both the control RNAi and *dyn-1(RNAi)*
359 representative images to enable better image presentation and viewing.

360 **For imaging embryos from the IYR038, IYR043, and IYR044 strains depicted in Figures 2-**
361 **5, Supplemental Figure S1, Supplemental Figure S2 and Supplemental Figure S3:**

362 A Nikon Ti2-E inverted microscope (Nikon Instruments Inc.) outfitted with a CREST X-Light
363 V3 spinning-disk confocal module, a motorized XY stage with encoder feedback, and a 600-µm
364 Z-piezo drive was used to make time-lapse videos of embryos. Embryos were dissected and
365 mounted on agarose pads, and coverslips were sealed with Vaseline following previously
366 described procedures (Bergwell, Smith, *et al.*, 2023). Laser illumination was supplied through a
367 Celesta solid-state light engine (Lumencor Inc.). Time-lapse image acquisition was performed in
368 NIS-Elements (Nikon Instruments Inc.), capturing 1.25-µm optical Z-stacks approximately every
369 35 seconds with a 60× Plan Apo λD oil-immersion objective (NA 1.42; refractive index 1.515)
370 and an ORCA-Fusion BT sCMOS detector (Hamamatsu Inc.). To ensure consistency in
371 quantitative measurements, all datasets were collected under identical exposure conditions: 200
372 msec exposure and 60% laser power at 561 nm and 400 msec exposure and 35% laser power at
373 488 nm. Maximum-intensity projections of Z-stacks were generated with NIS-Elements (Nikon
374 Instruments Inc.). For display purposes, brightness and contrast adjustments were applied
375 uniformly across the entire dataset.

376 **Spindle pole area measurement**

377 To measure spindle pole area, the cellSens software (Olympus America Inc.) was used to obtain
378 maximum intensity Z-projections of the original .vsi files. These Z-projections were saved in a
379 .png format with the fixed scaling (left:80 and right:400) for all images and further analyzed
380 using the Nikon NIS-Elements software (Nikon Instruments Inc.). The calibration on the NIS-

381 Elements software was set to 1 pixel = 0.18333 µm. The thresholding tool in NIS-Elements was
382 used to define and compute the spindle pole area (in μm^2) (intense mCherry::tubulin
383 fluorescence demarcated each spindle pole). Only regions with clearly defined spindle poles
384 were included in the analysis. Embryos in which spindle poles could not be reliably
385 distinguished were excluded. Brightness adjustments were equally applied to the images
386 representing spindle pole size in Figure 1A for better presentation and viewing.

387 **SPD-2 metaphase centrosome intensity measurements**

388 For measuring SPD-2 fluorescence intensity at centrosomes, the raw .vsi files acquired using
389 cellSens software (Olympus America Inc.) were opened in the Fiji software (Schindelin *et al.,*
390 2012) using the Bio-Formats importer plugin. The global scale was set to 1 pixel = 0.18333 µm.
391 Maximum-intensity Z-projections were generated and used for analyzing SPD-2 fluorescence
392 intensity at metaphase centrosomes. Metaphase was defined as the stage just prior to anaphase
393 onset, when the chromosomes had aligned at the cell center. A region of interest (ROI)
394 measuring 1033.33 $pixels^2$ was drawn around each metaphase centrosome and an adjacent area
395 of cytoplasm. The mean SPD-2 fluorescence intensity within each ROI (in arbitrary units, A.U.)
396 was quantified using the measure function in Fiji (Schindelin et al., 2012). Background SPD-2
397 fluorescence intensity (cytoplasmic ROI) was subtracted from the corresponding centrosomal
398 ROI value to obtain the final background-corrected SPD-2 centrosomal fluorescence intensity.
399 To calculate relative SPD-2 fluorescence levels normalized to control RNAi, all background-
400 corrected centrosomal fluorescence intensity values from both control RNAi and *dyn-1(RNAi)*
401 were divided by the mean background-corrected SPD-2 fluorescence intensity measured in
402 control RNAi embryos. Brightness, contrast, and sharpness adjustments were uniformly applied
403 to all images shown in Figure 1C to improve visualization of SPD-2 centrosome localization.

404 Embryos where the Z-projections did not capture the entire centrosome or where SPD-2 at the
405 centrosome could not be clearly identified due to surrounding debris were excluded from our
406 analysis.

407 **PLK-1 metaphase centrosome intensity measurements**

408 Metaphase was defined as the stage when the chromosomes had aligned at the center of the
409 metaphase plate. To quantify PLK-1::sfGFP fluorescence at the centrosomes, maximum intensity
410 Z-projections of metaphase embryos were generated and analyzed using Nikon NIS-Elements
411 software (Nikon Instruments Inc.). A region of interest (ROI) measuring 11.62 μm^2 was drawn
412 around each centrosome and within the cytoplasm of the same embryo. Cytoplasmic PLK-
413 1::sfGFP intensity was then subtracted from centrosomal PLK-1::sfGFP intensity to calculate the
414 background-corrected PLK-1::sfGFP centrosome fluorescence intensity, reported in arbitrary
415 units (A.U.). All background-corrected PLK-1::sfGFP centrosome intensities were divided by
416 the mean background-corrected PLK-1::sfGFP centrosome intensity of control embryos to
417 calculate the relative PLK-1 levels at centrosomes. Embryos with inaccurate PLK-1::sfGFP
418 fluorescence due to debris on top of the embryo affecting maximum intensity Z-projections or
419 instances where the Z-projections of the embryo did not cover the entire centrosome were
420 excluded from our analysis.

421 **Analysis of PLK-1 persistence at centrosomes**

422 To analyze PLK-1::sfGFP persistence at centrosomes at different cell cycle stages, maximum
423 intensity Z-projections of each timelapse sequence were quantified for centrosome-localized
424 PLK-1::sfGFP using the Nikon NIS-Elements software (Nikon Instruments Inc.). To quantify
425 centrosomal PLK-1::sfGFP levels across different cell-cycle stages, measurements were
426 restricted to the anterior centrosome. In the anterior cytoplasm, PLK-1::sfGFP background

427 fluorescence was relatively uniform, enabling consistent background subtraction and accurate
428 intensity quantification. By contrast, the posterior cytoplasm frequently exhibited irregular,
429 punctate PLK-1::sfGFP foci of variable sizes and intensities, which introduced inconsistency in
430 centrosome fluorescence measurements, especially at later cell cycle stages. For this reason,
431 posterior centrosomes were excluded from our quantitative analysis. The microtubule asters were
432 used to identify the position of the centrosomes at each cell cycle stage. A ROI of 11.62 μm^2 was
433 placed at the center of the asters as well as in its immediate vicinity (background). The PLK-
434 1::sfGFP fluorescence intensity at each anterior centrosome at every cell cycle stage was
435 determined by subtracting the background fluorescence intensity from the centrosomal
436 fluorescence intensity at that stage. Centrosomes with background-corrected PLK-1::sfGFP
437 fluorescence intensities greater than 5 arbitrary units (A.U.) were classified as "PLK-1 present"
438 whereas centrosomes with intensity values below this threshold were classified as "PLK-1
439 absent". The cell cycle stages were classified as follows: metaphase: a diamond-shaped spindle
440 formed and chromosomes aligned at the center, early anaphase: ~35 to 70 seconds after
441 metaphase when the chromosomes started separating, late anaphase: ~70 seconds after early
442 anaphase, early telophase: ~70 seconds after late anaphase, and 35 seconds after early telophase:
443 ~35 seconds after early telophase. In the occasional cases where PCM disassembly prevented
444 identification of the aster center, the centrosome position from the preceding frame was used as a
445 reference. Brightness adjustments were applied equally to the representative images in Figure 3A
446 for better presentation and viewing. Only embryos where the Z-projections captured the entire
447 centrosome were used for our analysis.

448 **Quantification of midbody abnormalities**

449 Maximum-intensity Z-projections generated using Nikon NIS-Elements (Nikon Instruments Inc.)
450 were used to analyze midbody defects. Embryos were scored in a randomized and blinded
451 manner: image files were renamed with randomized identifiers and scored by an independent
452 individual. The scorer evaluated IB behavior without knowledge of genotype or treatment until
453 scoring was complete. An intercellular bridge (IB) was defined as present when a continuous,
454 tubulin-intense connection between the two daughter cells could be clearly visualized. IB
455 assembly was used as an indicator of midbody formation (Hu *et al.*, 2012; Green *et al.*, 2013;
456 König *et al.*, 2017).

457 A normal IB was defined as one that started forming approximately 175–350 seconds
458 after metaphase onset, remained stable for at least 105 seconds following its formation, and
459 exhibited the stereotypical IB assembly dynamics. Stereotypical IB dynamics consisted of a
460 sequence in which the spindle midzone coalesced into a single focused, microtubule-rich bridge-
461 like IB structure. Following coalescence, the IB typically increased in tubulin intensity, then
462 gradually decreased in intensity as it regressed. Once coalesced, normal IBs did not separate or
463 fragment and maintained a continuous tubulin-dense morphology until midbody resolution.

464 An abnormal IB was defined as one that failed to exhibit this stereotypical progression.
465 Abnormal IBs included bridges that did not start forming within the 175–350 second window,
466 did not coalesce into a single focused structure, showed fluctuating tubulin intensity, or came
467 apart after coalescence. An embryo was scored as lacking an IB when no IB could be detected at
468 any point during the remainder of the cell cycle and through the onset of centrosome separation
469 in the next cell cycle.

470 Embryos where the entire IB was not captured in the maximum intensity Z-projections
471 were excluded from our analysis. For better visualization and presentation, brightness and
472 contrast setting were applied uniformly and equally to all the representative images in Figure 4A.

473 **Quantification of PLK-1 localization at the midbody**

474 PLK-1 localization at the midbody was quantified using a blinded, randomized analysis using
475 maximum intensity Z-projections that were generated with the Nikon NIS-Elements software
476 (Nikon Instruments Inc.). All image files were renamed with random alphanumeric identifiers by
477 an independent individual who was not involved in the scoring. The scorer analyzed the
478 randomized dataset without knowledge of genotype, treatment condition, or imaging sequence.
479 After all scoring was completed and recorded, the mapping key was revealed to assign quantified
480 values back to experimental groups.

481 An IB/midbody was defined as present when a continuous, tubulin-intense connection
482 between the two daughter cells could be clearly visualized in Z-projections. An IB was
483 considered to have formed if it remained cohesive for at least three consecutive frames (~105
484 seconds) after its appearance. Metaphase was defined as the timepoint immediately after nuclear
485 envelope breakdown when the chromosomes are aligned centrally at the metaphase plate. For
486 both time-matched and event-matched analyses, a normal PLK-1 localization pattern was defined
487 as a continuous, dot-like or band-like PLK-1::sfGFP signal above the local background at the IB
488 center. Abnormal localization was defined as discontinuous, fragmented, or off-center PLK-
489 1::sfGFP fluorescence, or signal that was indistinguishable from the local background. In the
490 time-matched analysis, cases in which PLK-1::sfGFP failed to localize to the IB either because
491 IB formation was delayed or because an IB did not assemble were also scored as abnormal. For
492 all analyses, PLK-1 localization was scored at the frame in which the IB was fully formed and

493 just before the tubulin intensity at the IB began to decrease, ensuring that measurements were
494 taken while the midbody remained structurally relatively intact.
495 For time-matched analysis, PLK-1::sfGFP fluorescence was assessed at the
496 developmental window when the IB normally started forming in control embryos (during the
497 reference window of 175–350 seconds after metaphase onset).
498 For event-matched analysis, PLK-1::sfGFP fluorescence was assessed whenever a stable
499 IB formed, even if the IB formed outside of the normal developmental window for bridge
500 assembly.
501 Z-projections in which either the IB or midbody-associated PLK-1 were not fully
502 captured across the Z-stack were excluded from analysis to ensure accurate evaluation of PLK-1
503 fluorescence at the IB/midbody. Brightness adjustments were applied equally to all
504 representative images of PLK-1 midbody localization in Figure 5A.
505 **Embryo size measurements**
506 Nikon-NIS Elements (Nikon Instruments Inc.) was used to generate maximum intensity Z-
507 projections of the raw data and to measure the sizes of metaphase-stage 1-cell *C. elegans*
508 embryos. To measure embryo size, the Bézier tool in NIS-Elements was used to manually trace
509 the outline of each embryo, using cytoplasmic PLK-1::sfGFP fluorescence to define the
510 cytoplasmic embryo boundary. The enclosed area was calculated by the software and reported in
511 μm^2. Embryos whose boundaries could not be clearly defined by cytoplasmic PLK-1::sfGFP
512 fluorescence due to embryo orientation were excluded from the analysis.
513 **Cytoplasmic PLK-1 fluorescence measurements**
514 Maximum intensity Z-projections generated by Nikon NIS-Elements (Nikon Instruments Inc.)
515 were used to measure cytoplasmic PLK-1::sfGFP in the anterior and posterior cytoplasm of wild-

516 type and *dyn-1(ky51)* embryos. For these measurements, the Z-projections were opened in NIS-
517 Elements and a large ROI of 128.97 μm^2 was placed within the anterior and posterior cytoplasm
518 of metaphase-stage embryos away from the spindle apparatus. The mean PLK-1::sfGFP
519 fluorescence intensities within these ROIs were determined using the NIS-Elements software and
520 reported in arbitrary units (A.U.). Measurements in which the ROI could not fit within the
521 embryo boundaries due to smaller embryo size were excluded from our analysis.

522 **Statistical analysis of *C. elegans* studies**

523 Graphpad prism 10.5 and 10.6.1 (GraphPad Software, Inc., San Diego, CA) were used to
524 perform statistical analyses of all the data. For all the data, error bars represent the standard
525 deviation (s.d.) above and below the mean and the middle lines represent the mean. *p*-values
526 were rounded to two decimal places and considered significant if $p<0.05$. A two-tailed unpaired
527 t-test was used to analyze: spindle pole area (Figure 1B), SPD-2 fluorescence intensity (Figure
528 1D), PLK-1::sfGFP centrosome fluorescence intensities at different cell cycle stages
529 (Supplemental Figure S3), *dyn-1* knockdown by RT-PCR (Supplemental Figure S1B), embryo
530 size (cytoplasmic area) (Supplemental Figure S1D), and cytoplasmic PLK-sfGFP intensity
531 (Supplemental Figure S2). A Fisher's exact test was used to analyze the PLK-1::sfGFP
532 persistence at the centrosomes (Figure 3B), and defects in PLK-1::sfGFP localization to the
533 midbody (Figure 5, B and C).

534 **ACKNOWLEDGMENTS**

535 This work was supported by NIH/NIGMS grants (5P20GM103636-09 and 7R15GM152965-02)
536 and start-up funding from North Carolina A&T State University to J.I. Additional support was
537 provided by NIH/NIGMS grant 1R35GM153737 and NCI grant 1R01CA273095 to R.N. We
538 would like to acknowledge Jasmyn Grant, Journey Reddick-Umoja, Erin Haastrup, Peter Nunan,

539 and Mariah Moreland for technical assistance. OC908 and OC779 strains were provided by Dr.
540 Kevin O'Connell (NIDDK, NIH). Some of the strains used in this study were provided by the
541 CGC, which is funded by NIH Office of Research Infrastructure Programs (P40 OD010440).
542 The authors declare no competing interests.

543 **REFERENCES**

544 Archambault V, Glover DM (2009). Polo-like kinases: conservation and divergence in their
545 functions and regulation. **Nat Rev Mol Cell Biol** *10*, 265–275.

546 Arnaud L, Pines J, Nigg EA (1998). GFP tagging reveals human Polo-like kinase 1 at the
547 kinetochore/centromere region of mitotic chromosomes. **Chromosoma** *107*, 424–429.

548 Barr FA, Silljé HHW, Nigg EA (2004). Polo-like kinases and the orchestration of cell division.
549 **Nat Rev Mol Cell Biol** *5*, 429–441.

550 Bergwell M, Smith A, Smith E, Dierlam C, Duran R, Haastrup E, Napier-Jameson R, Seidel R,
551 Potter W, Norris A, et al. (2023). A primary microcephaly-associated *sas-6* mutation perturbs
552 centrosome duplication, dendrite morphogenesis, and ciliogenesis in *Caenorhabditis elegans*.
553 **Genetics** *224*, iyad105.

554 Boxem M, Maliga Z, Klitgord N, Li N, Lemmens I, Mana M, De Lichtervelde L, Mul JD, Van
555 De Peut D, Devos M, et al. (2008). A protein domain-based interactome network for *C. elegans*
556 early embryogenesis. **Cell** *134*, 534–545.

557 Budirahardja Y, Gönczy P (2008). PLK-1 asymmetry contributes to asynchronous cell division
558 of *Caenorhabditis elegans* embryos. **Development** *135*, 1303–1313.

559 Chase D, Serafinas C, Ashcroft N, Kosinski M, Longo D, Ferris DK, Golden A (2000). The
560 polo-like kinase PLK-1 is required for nuclear envelope breakdown and the completion of
561 meiosis in *Caenorhabditis elegans*. **Genesis** *26*, 26–41.

562 Clark SG, Shurland DL, Meyerowitz EM, Bargmann CI, Van der Bliek AM (1997). A dynamin
563 GTPase mutation causes a rapid and reversible temperature-inducible locomotion defect in
564 *Caenorhabditis elegans*. **Proc Natl Acad Sci USA** *94*, 10438–10443.
565 Decker M, Jaensch S, Pozniakovsky A, Zinke A, O'Connell KF, Zachariae W, Myers E, and
566 Hyman AA (2011). Limiting amounts of centrosome material set centrosome size in *C. elegans*
567 embryos. **Curr Biol** *21*, 1259–1267.
568 Golsteyn RM, Mundt KE, Fry AM, Nigg EA (1995). Cell cycle regulation of the activity and
569 subcellular localization of Plk1, a human protein kinase implicated in mitotic spindle function. **J**
570 **Cell Biol** *129*, 1617–1628.
571 Gomez-Ferreria MA, Rath U, Buster DW, Chanda SK, Caldwell JS, Rines DR, Sharp DJ (2007).
572 Human Cep192 is required for mitotic centrosome and spindle assembly. **Curr Biol** *17*, 1960–
573 1966.
574 Grant B, Hirsh D (1999). Receptor-mediated endocytosis in the *Caenorhabditis elegans* oocyte.
575 **Mol Biol Cell** *10*, 4311–4326.
576 Green, R.A., J.R. Mayers, S. Wang, L. Lewellyn, A. Desai, A. Audhya, and K. Oegema (2013).
577 The midbody ring scaffolds the abscission machinery in the absence of midbody microtubules. **J**
578 **Cell Biol.** *203*, 505–520.
579 Hinshaw JE (2000). Dynamin and its role in membrane fission. **Annu Rev Cell Dev Biol** *16*,
580 483–519.
581 Hu CK, Coughlin M, Mitchison TJ (2012). Midbody assembly and its regulation during
582 cytokinesis. **Mol Biol Cell** *23*, 1024–1034.
583 Iyer J, Gentry LK, Bergwell M, Smith A, Guagliardo S, Kropp PA, Sankaralingam P, Liu Y,
584 Spooner E, Bowerman B, et al. (2022). The chromatin remodeling protein CHD-1 and the EFL-

585 1/DPL-1 transcription factor cooperatively downregulate CDK-2 to control SAS-6 levels and
586 centriole number. **PLoS Genet** *18*, e1009799.
587 Iyer J, DeVaul N, Hansen T, Nebenfuehr B (2019). Using microinjection to generate genetically
588 modified *Caenorhabditis elegans* by CRISPR/Cas9 editing. In: *Microinjection: Methods and*
589 *Protocols*, ed. C Liu and Y Du, New York, NY: Humana Press, 431–457.
590 Kamath RS, Ahringer J (2003). Genome-wide RNAi screening in *Caenorhabditis elegans*.
591 **Methods** *30*, 313–321.
592 Kemp CA, Kopish KR, Zipperlen P, Ahringer J, O'Connell KF (2004). Centrosome maturation
593 and duplication in *C. elegans* require the coiled-coil protein SPD-2. **Dev Cell** *6*, 511–523.
594 Kishi K, Van Vugt MA, Okamoto KI, Hayashi Y, Yaffe MB (2009). Functional dynamics of
595 Polo-like kinase 1 at the centrosome. **Mol Cell Biol** *29*, 3134–3150.
596 König J, Frankel EB, Audhya A, Müller-Reichert T (2017). Membrane remodeling during
597 embryonic abscission in *Caenorhabditis elegans*. **J Cell Biol** *216*, 1277–1286.
598 Lee KS, Yuan YL, Kuriyama R, Erikson RL (1995). Plk is an M-phase-specific protein kinase
599 and interacts with a kinesin-like protein, CHO1/MKLP1. **Mol Cell Biol** *15*, 7143–7151.
600 Levine MS, Holland AJ (2018). Impact of mitotic errors on cell proliferation and tumorigenesis.
601 **Genes Dev** *32*, 620–638.
602 Ly K, Reid SJ, Snell RG (2015). Rapid RNA analysis of individual *Caenorhabditis elegans*.
603 **MethodsX** *2*, 59–63.
604 Martino L, Morchoisne Bolhy S, Cheerambathur DK, Van Hove L, Dumont J, Joly N, Desai A,
605 Doye V, Pintard L (2017). Channel nucleoporins recruit PLK-1 to nuclear pore complexes to
606 direct nuclear envelope breakdown in *C. elegans*. **Dev Cell** *43*, 157–171.

607 O'Connell KF, Maxwell KN, White JG (2000). The *spd-2* gene is required for axis polarization
608 in the *C. elegans* zygote. **Dev Biol** *222*, 55–70.
609 Paix A, Folkmann A, Rasoloson D, Seydoux G (2015). High efficiency, homology-directed
610 genome editing in Caenorhabditis elegans using CRISPR-Cas9 ribonucleoprotein complexes.
611 **Genetics** *201*, 47–54.
612 Paix A, Schmidt H, Seydoux G (2016). Cas9-assisted recombineering in *C. elegans*: genome
613 editing using in vivo assembly of linear DNAs. **Nucleic Acids Res** *44*, e128.
614 Paschal BM, Shpetner HS, Vallee RB (1987). MAP 1C is a microtubule-activated ATPase which
615 translocates microtubules in vitro and has dynein-like properties. **J Cell Biol** *105*, 1273–1282.
616 Pelletier L, Özlü N, Hannak E, Cowan C, Habermann B, Ruer M, Müller-Reichert T, Hyman AA
617 (2004). The *Caenorhabditis elegans* centrosomal protein SPD-2 is required for both
618 pericentriolar material recruitment and centriole duplication. **Curr Biol** *14*, 863–873.
619 Petronczki M, Lénárt P, Peters JM (2008). Polo on the rise—from mitotic entry to cytokinesis
620 with Plk1. **Dev Cell** *14*, 646–659.
621 Praefcke GJA, McMahon HT (2004). The dynamin superfamily: universal membrane tubulation
622 and fission molecules?. **Nat Rev Mol Cell Biol** *5*, 133–147.
623 Schindelin J, Arganda-Carreras I, Frise E, Kaynig V, Longair M, Pietzsch T, Preibisch S,
624 Rueden C, Saalfeld S, Schmid B, Tinevez J-Y, et al. (2012). Fiji: an open-source platform for
625 biological-image analysis. **Nat Methods** *9*, 676–682.
626 Schmucker S, Sumara I (2014). Molecular dynamics of PLK1 during mitosis. **Mol Cell Oncol** 1,
627 e954507.
628 Shpetner HS, Vallee RB (1989). Identification of dynamin, a novel mechanochemical enzyme
629 that mediates interactions between microtubules. **Cell** *59*, 421–432.

630 Smith A, Bergwell M, Smith E, Mathew D, Iyer J (2020). CRISPR/Cas9 editing of the *C.*
631 *elegans rbm-3.2* gene using the *dpy-10* Co-CRISPR screening marker and assembled
632 ribonucleoprotein complexes. **J Vis Exp** *166*, e62001.
633 Sugioka K, Hamill DR, Lowry JB, McNeely ME, Enrick M, Richter AC, Kiebler LE, Priess JR,
634 Bowerman B (2017). Centriolar SAS-7 acts upstream of SPD-2 to regulate centriole assembly
635 and pericentriolar material formation. **eLife** *6*, e20353.
636 Thompson HM, Skop AR, Euteneuer U, Meyer BJ, McNiven MA (2002). The large GTPase
637 dynamin associates with the spindle midzone and is required for cytokinesis. **Curr Biol** *12*,
638 2111–2117.
639 Zhu F, Lawo S, Bird A, Pinchev D, Ralph A, Richter C, Müller-Reichert T, Kittler R, Hyman
640 AA, Pelletier L (2008). The mammalian SPD-2 ortholog Cep192 regulates centrosome
641 biogenesis. **Curr Biol** *18*, 136–141.
642 Zitouni S, Nabais C, Jana SC, Guerrero A, Bettencourt-Dias M (2014). Polo-like kinases:
643 structural variations lead to multiple functions. **Nat Rev Mol Cell Biol** *15*, 433–452.

644 **FIGURE LEGENDS**

645 FIGURE 1. DYN-1 depletion increases spindle pole size and elevates SPD-2 at centrosomes. (A)
646 Spindle pole morphology in embryos expressing mCherry::tubulin, showing enlarged spindle
647 poles upon *dyn-1(RNAi)*. White arrows: spindle poles. (B) Quantification of spindle pole area
648 using mCherry::tubulin fluorescence. Each point = single pole; n = spindle poles analyzed. Error
649 bars = s.d.; middle bar = mean. (C) SPD-2 localization at metaphase centrosomes in control and
650 *dyn-1(RNAi)* embryos. Dotted outline demarcates the embryo boundary; white arrows:
651 centrosome-localized SPD-2 (D) Relative centrosomal SPD-2 intensity normalized to control

652 RNAi. n = centrosomes. Error bars = s.d.; middle bar = mean. (B, D): unpaired two-tailed t-test;
653 Experimental replicates: 4 for all assays. All fluorescence images include a 10 µm scale bar.
654
655 FIGURE 2. DYN-1 depletion increases centrosomal PLK-1 at metaphase. (A) PLK-1::sfGFP
656 localization at metaphase centrosomes in control RNAi vs *dyn-1(RNAi)* embryos. White arrows:
657 centrosome-localized PLK-1::sfGFP. (B) Quantification of PLK-1::sfGFP centrosomal
658 fluorescence at metaphase. n = centrosomes. Error bars = s.d.; middle bar = mean. (C) PLK-
659 1::sfGFP localization in wild-type (wt) *dyn-1* and *dyn-1(ky51)*. White arrows: centrosome-
660 localized PLK-1::sfGFP. (D) Relative centrosomal PLK-1 intensity in wild-type (wt) *dyn-1* and
661 *dyn-1(ky51)*. n = centrosomes. Error bars = s.d.; middle bar = mean. (B, D): unpaired two-tailed
662 t-test; Experimental replicates: 3 for all assays. All fluorescence images include a 10 µm scale
663 bar.
664
665 FIGURE 3. PLK-1 persists abnormally at centrosomes during mitotic progression in *dyn-*
666 *1(RNAi)* embryos. (A) Time-lapse analysis of different mitotic stages in control RNAi and *dyn-*
667 *1(RNAi)* embryos. White arrows: anterior centrosome-localized PLK-1::sfGFP. (B) Percentage
668 of centrosomes retaining PLK-1 at each stage. Fisher's Exact Test; n = centrosomes analyzed.
669 Experimental replicates: 3 for all assays. All fluorescence images include a 10 µm scale bar.
670
671 FIGURE 4. DYN-1 depletion disrupts Intercellular Bridge (IB) assembly. (A) Time-lapse images
672 of mCherry::tubulin showing normal IB formation in control RNAi embryos (top panel) and
673 abnormal (middle panel) or missing (bottom panel) IBs in *dyn-1(RNAi)* embryos. White arrows:

674 IB (B) Classification of IB morphology (normal, abnormal, absent). n = embryos analyzed.
675 Experimental replicates: 3 for all assays. All fluorescence images include a 10 µm scale bar.
676
677 FIGURE 5. PLK-1 localization at the midbody is defective in *dyn-1(RNAi)* embryos. (A) Time-
678 matched and event-matched PLK-1::sfGFP localization at the midbody in control RNAi and *dyn-*
679 *1(RNAi)* embryos. White arrows: IB; yellow arrows: PLK-1::sfGFP at IB (B) Time-matched
680 PLK-1 scoring at the midbody. n = embryos; Fisher's Exact Test. (C) Event-matched PLK-1
681 scoring at the midbody. n = embryos; Fisher's Exact Test. Experimental replicates: 3 for all
682 assays. All fluorescence images include a 10 µm scale bar.
683 **SUPPLEMENTAL FIGURES**
684 FIGURE S1. *dyn-1(RNAi)* reduces *dyn-1* mRNA levels and decreases embryo size. (A) RT-PCR
685 validation of *dyn-1* depletion. (B) Relative *dyn-1* mRNA quantification. Error bars = s.d.; middle
686 bar = mean. (C) Comparison of average embryo sizes in control RNAi and *dyn-1(RNAi)*. (D)
687 Cytoplasmic area quantification using PLK-1::sfGFP fluorescence as a marker for the
688 cytoplasmic embryo border. n = embryos. Error bars = s.d. (B, D): unpaired two-tailed t-test;
689 Experimental replicates: 3 for all assays. All fluorescence images include a 10 µm scale bar.
690
691 FIGURE S2. Cytoplasmic PLK-1::sfGFP levels are modestly elevated in *dyn-1(ky51)* embryos as
692 compared to wild-type. (A) Quantification of anterior and posterior cytoplasmic PLK-1::sfGFP
693 in wild-type (wt) *dyn-1* and *dyn-1(ky51)* embryos. A.U.= Arbitrary Units; unpaired two-tailed t-
694 test; n = measurements. Error bars = s.d.; middle bar = mean. Experimental replicates: 3. All
695 fluorescence images include a 10 µm scale bar.
696

697 FIGURE S3. Comparison of centrosomal PLK-1 intensity across cell cycle stages in control
698 RNAi and *dyn-1(RNAi)* embryos. (A) Centrosomal PLK-1::sfGFP intensity at metaphase, early
699 and late anaphase, early telophase, and 35 seconds post early telophase. A.U.= Arbitrary Units;
700 unpaired two-tailed t-test; n = 29 centrosomes (control RNAi); n = 26 centrosomes (*dyn-*
701 *1(RNAi))*. Error bars = s.d.; middle bar = mean. Experimental replicates: 3. All fluorescence
702 images include a 10 µm scale bar.
703

Figure 1

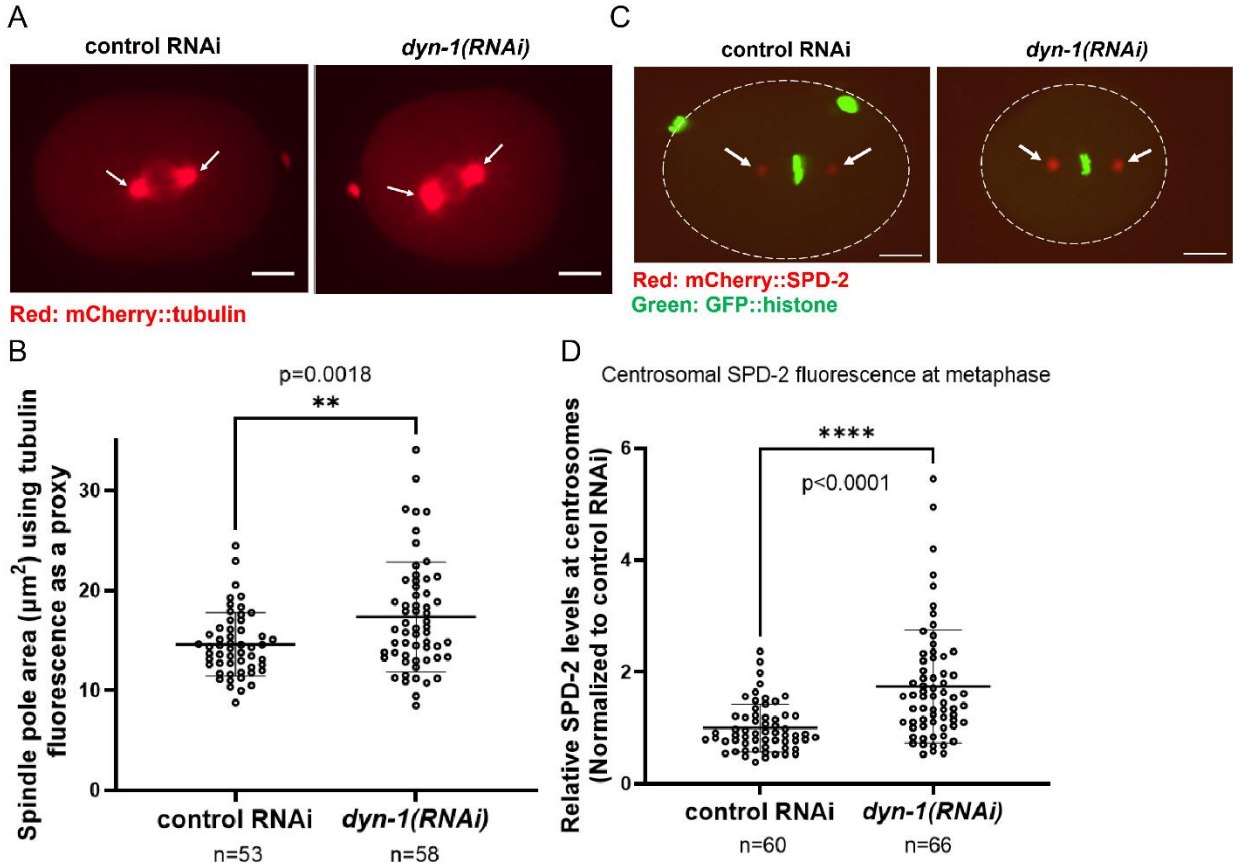
A
control RNAi
dyn-1(RNAi)
Red: mCherry::tubulin
C
control RNAi
dyn-1(RNAi)
Red: mCherry::SPD-2
Green: GFP::histone
B
p=0.0018
**
Spindle pole area (μm²) using tubulin fluorescence as a proxy
0
10
20
30
control RNAi
dyn-1(RNAi)
n=53
n=58
D
Centrosomal SPD-2 fluorescence at metaphase
****
p<0.0001
Relative SPD-2 levels at centrosomes (Normalized to control RNAi)
0
2
4
6
control RNAi
dyn-1(RNAi)
n=60
n=66

Figure 2

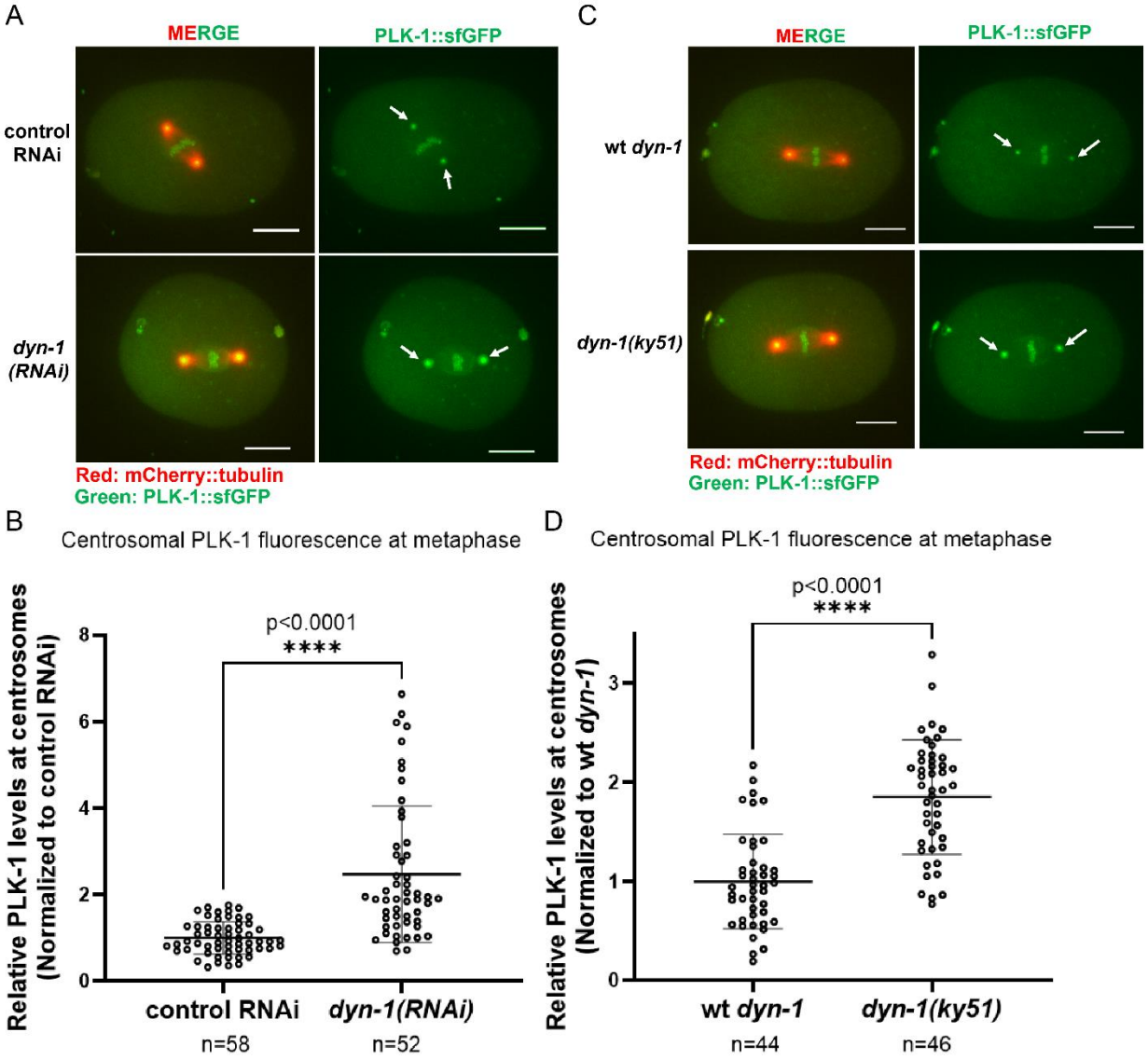
A
MERGE
PLK-1::sfGFP
control RNAi
dyn-1 (RNAi)
Red: mCherry::tubulin
Green: PLK-1::sfGFP
C
MERGE
PLK-1::sfGFP
wt dyn-1
dyn-1(ky51)
Red: mCherry::tubulin
Green: PLK-1::sfGFP
B
Centrosomal PLK-1 fluorescence at metaphase
Relative PLK-1 levels at centrosomes (Normalized to control RNAi)
p<0.0001
****
control RNAi
dyn-1(RNAi)
n=58
n=52
D
Centrosomal PLK-1 fluorescence at metaphase
Relative PLK-1 levels at centrosomes (Normalized to wt dyn-1)
p<0.0001
****
wt dyn-1
dyn-1(ky51)
n=44
n=46

Figure 3

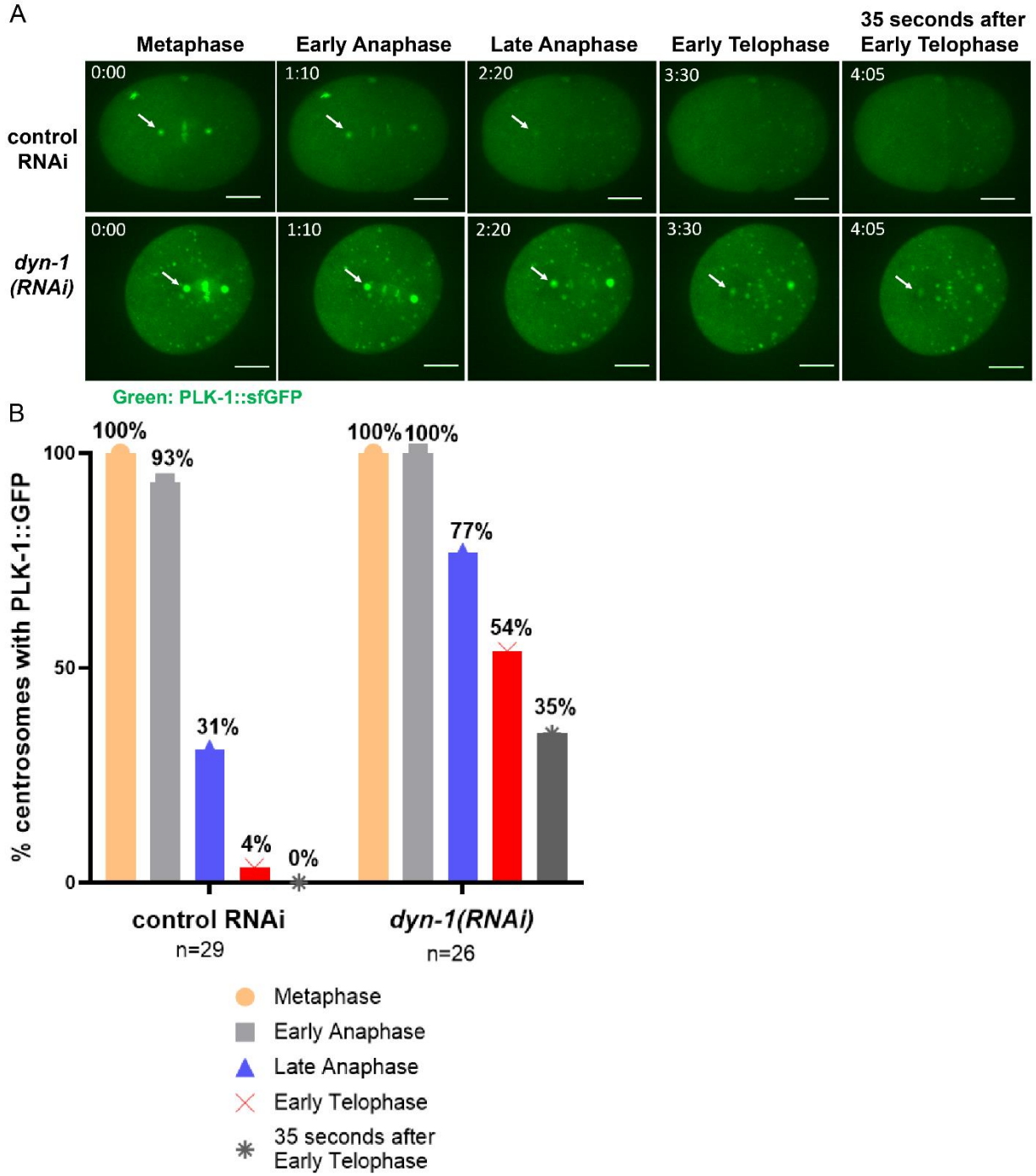
A
Metaphase
Early Anaphase
Late Anaphase
Early Telophase
35 seconds after Early Telophase
control RNAi
dyn-1 (RNAi)
0:00
1:10
2:20
3:30
4:05
Green: PLK-1::sfGFP
B
% centrosomes with PLK-1::GFP
100
50
0
100%
93%
31%
4%
0%
100%
100%
77%
54%
35%
control RNAi
n=29
dyn-1(RNAi)
n=26
Metaphase
Early Anaphase
Late Anaphase
Early Telophase
35 seconds after Early Telophase

Figure 4

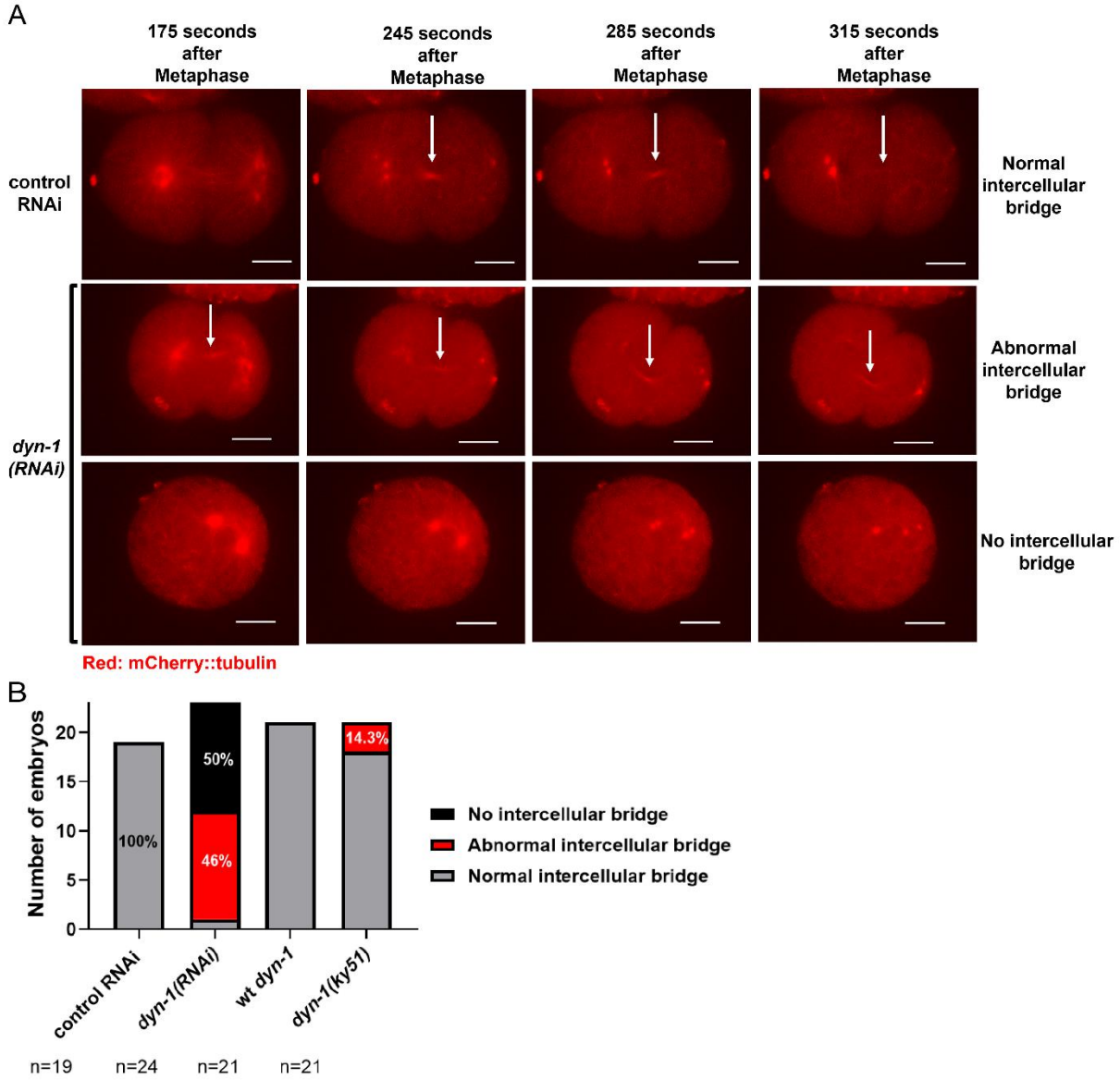
A
175 seconds after Metaphase
245 seconds after Metaphase
285 seconds after Metaphase
315 seconds after Metaphase
control RNAi
dyn-1 (RNAi)
Normal intercellular bridge
Abnormal intercellular bridge
No intercellular bridge
Red: mCherry::tubulin
B
Number of embryos
0
5
10
15
20
100%
50%
46%
14.3%
No intercellular bridge
Abnormal intercellular bridge
Normal intercellular bridge
control RNAi
dyn-1(RNAi)
wt dyn-1
dyn-1(ky51)
n=19
n=24
n=21
n=21

Figure 5

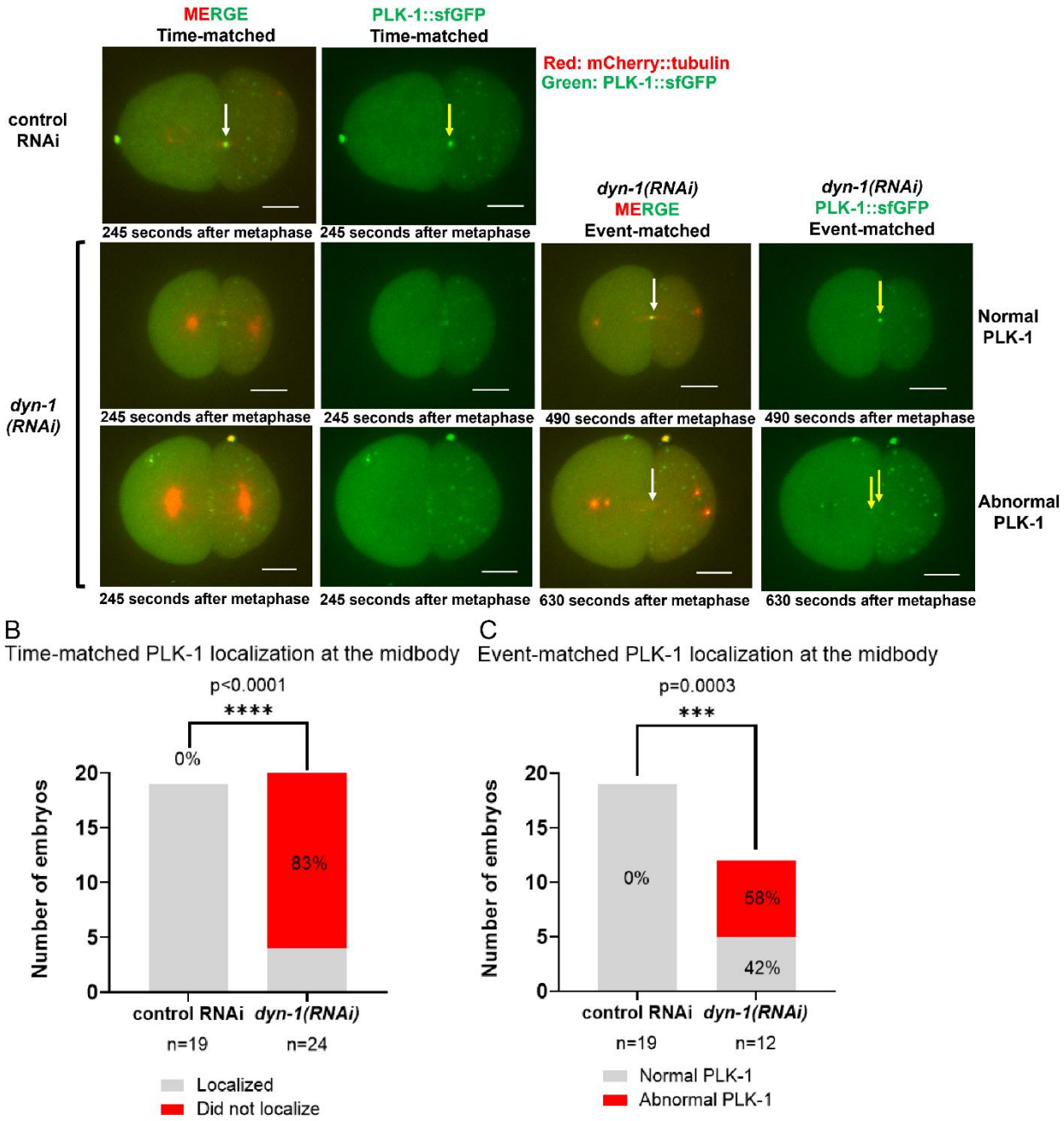
MERGE
Time-matched
PLK-1::sfGFP
Time-matched
Red: mCherry::tubulin
Green: PLK-1::sfGFP
control RNAi
245 seconds after metaphase
245 seconds after metaphase
dyn-1(RNAi)
MERGE
Event-matched
dyn-1(RNAi)
PLK-1::sfGFP
Event-matched
dyn-1 (RNAi)
Normal PLK-1
245 seconds after metaphase
245 seconds after metaphase
490 seconds after metaphase
490 seconds after metaphase
Abnormal PLK-1
245 seconds after metaphase
245 seconds after metaphase
630 seconds after metaphase
630 seconds after metaphase
B
Time-matched PLK-1 localization at the midbody
p<0.0001
****
0%
83%
Number of embryos
control RNAi
dyn-1(RNAi)
n=19
n=24
Localized
Did not localize
C
Event-matched PLK-1 localization at the midbody
p=0.0003
***
0%
58%
42%
Number of embryos
control RNAi
dyn-1(RNAi)
n=19
n=12
Normal PLK-1
Abnormal PLK-1